Lattice Resonances of Nanohole Arrays for Quantum Enhanced Sensing

Stephen Sanders[,1] Mohammadjavad Dowran,[2,3] Umang Jain[,2,3] Tzu-Ming Lu[,4]
Alberto M. Marino[,2,3,*] and Alejandro Manjavacas[1,5,†]

[1] *Department of Physics and Astronomy, University of New Mexico, Albuquerque, New Mexico 87106, USA*
[2] *Homer L. Dodge Department of Physics and Astronomy, The University of Oklahoma, 440 W. Brooks St., Norman, Oklahoma 73019, USA*
[3] *Center for Quantum Research and Technology (CQRT), The University of Oklahoma, Norman, Oklahoma 73019, USA*
[4] *Center for Integrated Nanotechnologies, Sandia National Laboratories, Albuquerque, New Mexico 87123, USA*
[5] *Instituto de Óptica (IO-CSIC), Consejo Superior de Investigaciones Científicas, Madrid 28006, Spain*

Periodic arrays of nanoholes perforated in metallic thin films interact strongly with light and produce large electromagnetic near-field enhancements in their vicinity. As a result, the optical response of these systems is very sensitive to changes in their dielectric environment, thus making them an exceptional platform for the development of compact optical sensors. Given that these systems already operate at the shot-noise limit when used as optical sensors, their sensing capabilities can be enhanced beyond this limit by probing them with quantum light, such as squeezed or entangled states. Motivated by this goal, here, we present a comparative theoretical analysis of the quantum enhanced sensing capabilities of metallic nanohole arrays with one and two holes per unit cell. Through a detailed investigation of their optical response, we find that the two-hole array supports resonances that are narrower and stronger than its one-hole counterpart, and therefore have a higher fundamental sensitivity limit as defined by the quantum Cramér-Rao bound. We validate the optical response of the analyzed arrays with experimental measurements of the reflectance of representative samples. The results of this work advance our understanding of the optical response of these systems and pave the way for developing sensing platforms capable of taking full advantage of the resources offered by quantum states of light.

I. INTRODUCTION

Periodic arrays of nanoholes drilled in metallic films support lattice resonances arising from the coherent interaction between the localized surface plasmons supported by the individual holes [1,2]. These resonances appear at wavelengths commensurate with the periodicity of the array and, due to their collective nature, give rise to strong and spectrally narrow optical responses, which result in quality factors much larger than those of the localized plasmons of the individual holes [1–3]. Lattice resonances are at the origin of the phenomenon known as extraordinary optical transmission (EOT) [1,4–6], in which nanohole arrays display transmittance orders of magnitude larger than the predictions of classical aperture theory [7]. Thanks to these properties, periodic arrays of nanoholes have emerged as an ideal platform for the development of a variety of applications including nanoscale light emission [8,9], color filtering and printing [10,11],

multispectral imaging [12], and second-harmonic generation [13].

Of particular interest is the use of these systems as optical sensors [14–21]. The strong field enhancements produced by the lattice resonances in the vicinity of the array, together with their large quality factors, enable the detection of small variations in the dielectric environment of the array through the measurement of changes in its optical response. For these reasons, metallic nanohole arrays are being used to detect, for instance, biomolecules [22] and viruses [23]. However, even for an ideal optical sensor, the sensing threshold is ultimately limited by the properties of the light used to probe it. When using a classical electromagnetic field, this threshold is manifested as the shot-noise limit [24]. Therefore, the only way to increase the sensitivity of a given optical sensor without using more photons (i.e., increasing the intensity of light) is by extracting more information from each photon [25–27]. This goal can be achieved through the use of quantum states of light, such as squeezed or entangled states, as was originally proposed and later demonstrated for interferometry applications [28–31]. More recently, it has been shown

*marino@ou.edu
†a.manjavacas@csic.es

that plasmonic structures can preserve the quantum properties of light [32–36], which has led to the development of different quantum enhanced plasmonic sensors capable of achieving sensitivities beyond the shot-noise limit [37–41]. Periodic arrays of nanoholes are particularly suited for this goal, as recently demonstrated [42]. However, in order to better exploit the additional resources provided by quantum states of light, it is necessary to adequately engineer the optical response of the nanohole arrays.

In this paper, we present a comprehensive theoretical analysis of the optical response of periodic arrays of nanoholes perforated in metal films, with the focus on understanding how they can be designed to take full advantage of the quantum resources provided by squeezed light. In particular, we investigate the reflectance spectra of nanohole arrays perforated in gold films with either one or two holes per unit cell. This geometry is simple enough to enable accurate fabrication, while still allowing us to study the impact of multiple holes and symmetry breaking in the same unit cell. We explore the effect that the different geometrical parameters have on the optical response of these systems and find that two-hole arrays support narrower lattice resonances that lead to more pronounced dips in reflectance, and, therefore, are better suited for sensing applications. We verify these theoretical predictions by measuring the reflectance of representative sample arrays fabricated using electron-beam lithography and metal lift off. With the knowledge of the optical response of the arrays, we calculate fundamental sensitivity bounds that can, in principle, be achieved if the arrays are illuminated with squeezed states of light. We analyze these fundamental sensitivity bounds for certain levels of squeezing, as well as the effective enhancement with respect to the sensitivity obtained using classical illumination. Our work provides valuable insight for the design of plasmonic sensors based on nanohole arrays capable of exploiting the quantum resources of squeezed light to achieve detection thresholds beyond the classical limit.

II. RESULTS

The systems under study consist of periodic arrays of circular nanoholes with diameter D drilled in gold films of thickness t, which are placed on top of silicon substrates. We consider arrays with one and two holes per unit cell, as shown in Figs. 1(a) and 1(b). The arrays have a rectangular unit cell with periods along the x and y axes given, respectively, by a and b. In the case of the two-hole array, the center-to-center distance between the holes is d. The arrays are excited with an electromagnetic plane wave of wavelength λ, traveling along the negative z axis, with a magnetic field of amplitude H_0 polarized along the y axis. To calculate the optical response of the arrays, we rigorously solve Maxwell's equations using a finite-element-method
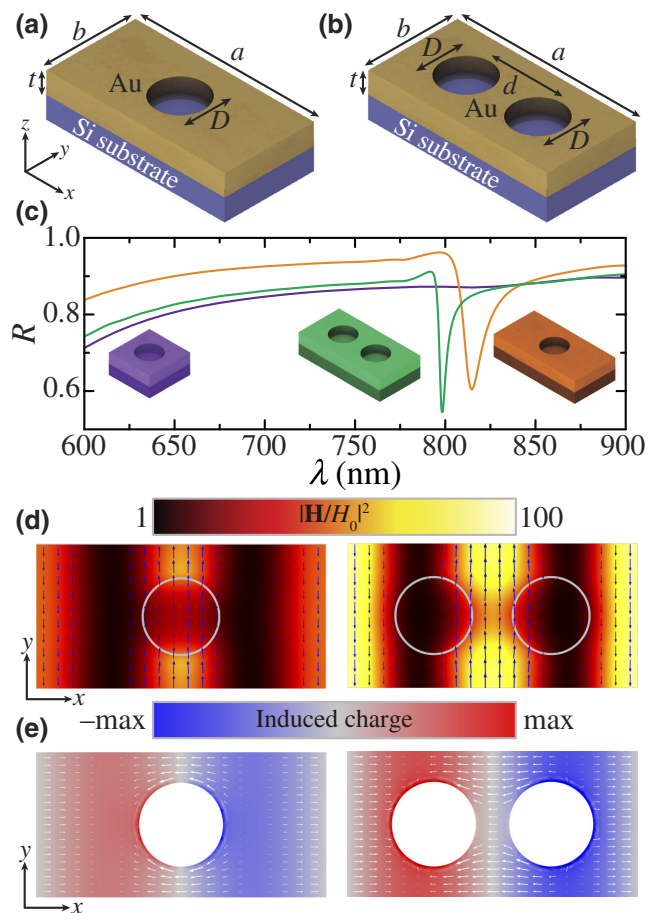

FIG. 1. (a), (b) Schematics of the periodic arrays of circular nanoholes under consideration with one (a) and two (b) holes per unit cell. (c) Calculated reflectance spectra for arrays with periods $a = 784$ nm and $b = a/2$, with one (orange curve) and two (green curve) holes per unit cell. In both cases, the thickness of the gold film is $t = 80$ nm and the diameter of the holes is $D = 210$ nm. For the two-hole array, the center-to-center distance between the holes is $d = 315$ nm. For comparison, we also plot the reflectance spectrum of a two-hole array with $d = a/2 = b$ (purple curve). Notice that this array is equivalent to a one-hole array with a square unit cell with period b along the x and y axes. (d) Magnetic field calculated 20 nm above the array surface, at the resonance wavelength of the one- (orange curve, $\lambda = 815$ nm) and two-hole (green curve, $\lambda = 798$ nm) arrays of (c). The color encodes the magnitude of the enhancement, while the arrows indicate the direction of the magnetic field. (e) Induced surface charge (color plot) and current (arrow plot) on the top surface of the one- and two-hole arrays calculated at the same wavelengths as in panel (d).

(FEM) approach implemented in the commercial software COMSOL Multiphysics (see Appendix A for details).

We envision a sensing protocol in which the variations of the dielectric environment above the array are detected through the measurement of changes in its reflectance. Therefore, the ideal nanohole array would have an optical

response that, around the wavelength of operation, displays both a steep slope and a large reflectance. This can be achieved by designing a nanohole array that supports a lattice resonance in the relevant spectral range. For normal incidence, the longest-wavelength lattice resonance supported by a periodic array appears at a wavelength slightly larger than the largest periodicity [1]. Based on that, we choose the arrays to have a periodicity $a = 784$ nm and $b = a/2$. This ensures that their lattice resonances are located around $\lambda \approx 800$ nm, which corresponds to the wavelength used in previous quantum enhanced plasmonic sensing experiments [42].

Figure 1(c) shows the calculated reflectance spectrum for a one- (orange curve) and two-hole (green curve) array. In both cases, the diameter of the circular holes is $D = 210$ nm and the thickness of the gold film is $t = 80$ nm. For the two-hole array, the center-to-center distance between the holes is $d = 315$ nm. This value of d ensures that the holes are well separated and, together with the values of the other parameters, makes it possible to fabricate high-quality arrays. As anticipated, both arrays display a lattice resonance around $\lambda = a$, which results in a narrow dip in the reflectance spectrum. The dip is sharper and more pronounced for the two-hole array, and its minimum is located at shorter wavelengths. Expectedly, for the two-hole array, the characteristics of its lattice resonance depend strongly on the distance between the holes, as we explore further below. In particular, when $d = a/2 = b$, the system becomes a one-hole array with a square unit cell with period b along the x and y axes [see the purple inset to Fig. 1(c)]. Consequently, its reflectance spectrum, indicated by the purple curve, does not show any features in the range of wavelengths under consideration, since its longest-wavelength lattice resonance is located at $\lambda \approx b$.

In order to gain insight into the physical origin of the lattice resonances supported by the nanohole arrays, we analyze both the magnetic field and the induced surface charge in the unit cell at the resonance wavelength. In particular, the color maps in Fig. 1(d) represent the enhancement of the magnetic field intensity on a plane parallel to the array located 20 nm above it, while the arrows indicate the direction of the field. In both cases, the magnetic field oscillates along the x axis with a period a and is almost uniform along the y axis, exactly as expected for the longest-wavelength lattice resonance of a periodic system [43,44]. By examining the magnetic field around the hole of the one-hole array, we observe that it is similar to that of a magnetic dipole oriented along the y axis, which is consistent with previous studies of the response of holes in metallic films under normal incidence illumination [1,45]. This is further supported by the corresponding induced surface charge (color plot) and current (arrows) displayed in Fig. 1(e). Interestingly, analyzing all of these quantities for the two-hole array, we observe that, in that case, the two holes give rise to a single effective magnetic dipole. This

closely resembles the lattice resonances with subradiant character investigated in periodic arrays of nanoparticles with two-particle unit cells [46]. Such resonances emerge in the spectrum as a result of a symmetry breaking in the geometry of the array that results in a partial cancellation of the radiation produced by each of the elements in the unit cell. As a consequence, these resonances present a subradiant or dark character that leads to reduced radiative losses, which, in turn, produce much sharper spectral features than standard lattice resonances [46,47]. In the nanohole arrays considered here, the symmetry breaking is produced by d being different from $a/2$, which transforms an array with one hole in a square unit cell into an array with two holes in a rectangular unit cell. As a result of this, the two-hole array displays a sharper and more pronounced dip in reflectance than the one-hole array with rectangular unit cell, thus making it a better platform for sensing applications. Notice that other symmetry-breaking mechanisms, such as the use of two holes with different diameters, have been investigated in the past for nanohole arrays perforated in a silicon film [48]. Besides this, there are many more available mechanisms that have been proposed and investigated to reduce radiative losses, including the use of bound states in the continuum, anapole modes, and topological phases [49,50]. This opens the possibility for the design of more complicated geometries that could produce even narrower resonances.

To complete the characterization of the nanohole arrays, we investigate the impact that the hole diameter, the gold-film thickness, and the center-to-center separation have on their optical response. Figure 2 shows the reflectance spectrum of one- and two-hole arrays with $a = 784$ nm, $b = a/2$, and different values of D, t, and d, as indicated by the legends. In particular, Figs. 2(a)–(d) analyze the effect of varying the diameter of the holes. Examining these results, we observe that for all cases, an increase in D results in a more pronounced dip in reflectance. However, while for the one-hole array the dip shifts to longer wavelengths as D grows, as shown in Fig. 2(a), the opposite is true for the two-hole arrays, as shown in Figs. 2(b)–(d). This difference can be attributed to the more complex response of the two-hole unit cell, which is determined not only by the size of the holes but also by the separation between them. Indeed, comparing the results of Figs. 2(b)–(d), we observe that as d grows and approaches $a/2$, the reflectance dip both becomes weaker and shifts towards shorter wavelengths.

The effect of the thickness of the gold film in the reflectance of the arrays is analyzed in Figs. 2(e)–(h). We observe that, for all of the arrays under consideration, an increase in t has two main effects, both of which arise from the increase of free carriers in the system. First, it results in a more pronounced reflectance dip. Second, it makes the reflectance outside the lattice resonance approach unity. Therefore, the combination of these two effects contributes to obtain a reflectance spectrum with steeper features.
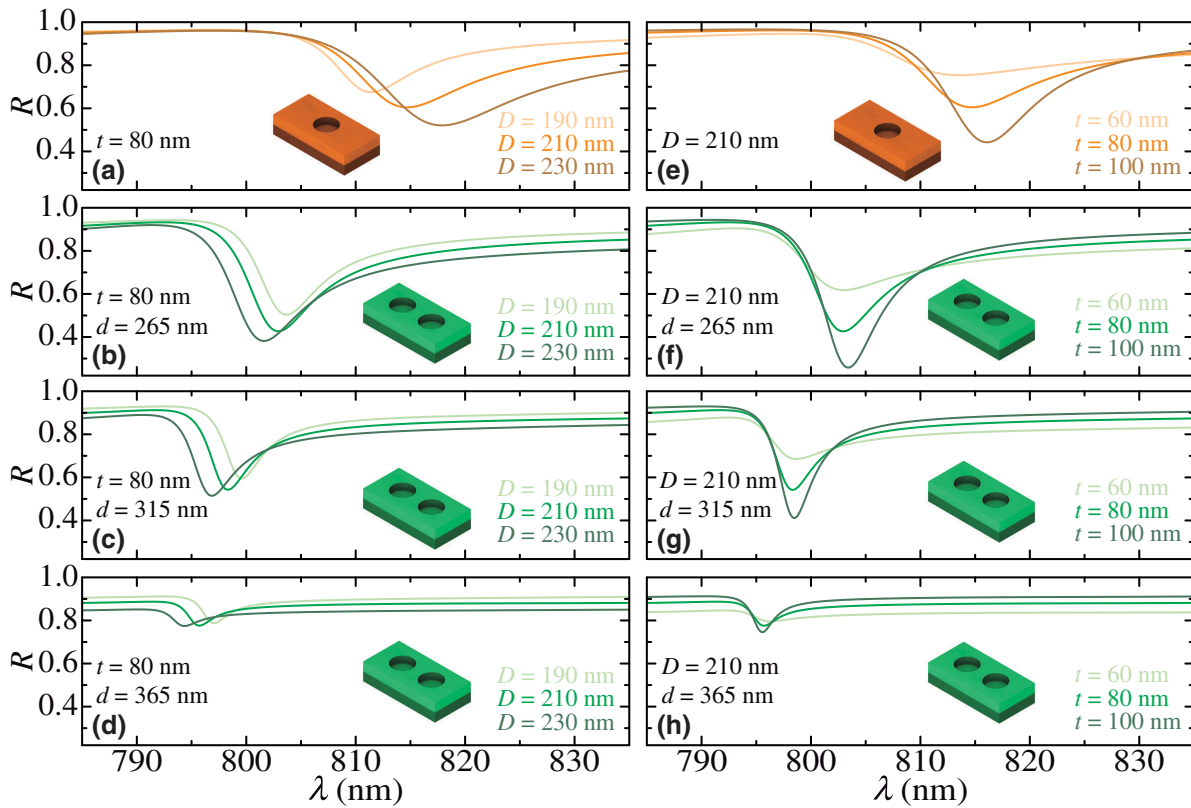
FIG. 2. Reflectance spectra for one- and two-hole arrays with periods $a = 784$ nm, $b = a/2$, and different values of hole diameter D, gold-film thickness t, and distance between holes d, as indicated in the legends.

However, it is expected that this behavior saturates as t becomes significantly larger than the skin depth of gold.

In order to validate our theoretical calculations, we fabricate three representative nanohole arrays and measure their reflectance spectra (see Appendices B and C for details). The corresponding results are plotted in Fig. 3 with solid curves. The SEM images on the right show representative areas of the different arrays fabricated (the scale bars correspond to 1.5 μm). We compare the experimental measurements with theoretical calculations (dashed curves), which are performed using the averaged values of the different geometrical parameters extracted from a statistical analysis of the SEM images using the image analysis package of MATLAB. The uncertainty in the value of the extracted parameters is always below 2%. In all of the cases, the thickness of the gold film is $t = 80$ nm. Panel (a) shows the reflectance spectrum for a one-hole array with geometrical parameters $D = 171$ nm, $a = 781$ nm, and $b = 389$ nm, as extracted from the SEM images. The theoretical calculations using these parameters predict a dip around 800 nm, which is in very good agreement with the experimental measurements considering the absence of free parameters in the theoretical calculations. As expected from our previous analysis, the dip in reflectance becomes sharper and more pronounced for the two-hole array

analyzed in panel (b), for which $D = 204$ nm, $a = 781$ nm, $b = 389$ nm, and $d = 310$ nm. Again, the experimental results are in very good agreement with the theoretical calculations. In both panels, the small differences between the theoretical calculations and the measurements can be attributed to fabrication imperfections as well as finite-size effects [51]. To complete the cases analyzed in Fig. 1(c), we show, in Fig. 3(c), the results for a two-hole array with $D = 208$ nm, $a = 781$ nm, $b = 389$ nm, and $d = 391$ nm. Since $d \approx a/2$, this system is effectively a one-hole array with a square unit cell with period b along the x and y axes. Therefore, it does not support any lattice resonance in the spectral region under consideration, as confirmed by both the experimental measurements and the theoretical calculations. The experimental measurements shown in Fig. 3 serve to validate our theoretical analysis and confirm that the symmetry breaking in arrays with two holes per unit cell leads to sharper lattice resonances.

Having completed the characterization of the optical response of the nanohole arrays, we are now equipped to investigate the sensitivity that they can reach when used as optical sensors to detect small changes in the refractive index of the dielectric environment above them. The sensitivity S of such a sensor is defined as the inverse of the smallest change in the refractive index that it can detect,
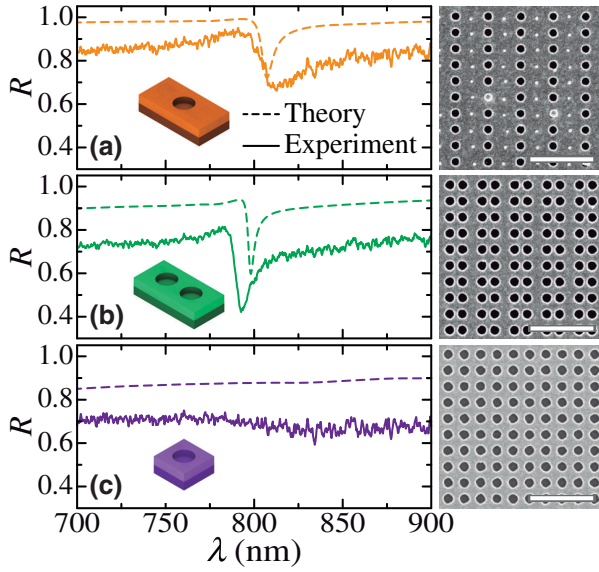
FIG. 3. Comparison between experimental measurements of the reflectance spectrum (solid curves) and the corresponding theoretical calculations (dashed curves). The specific parameters for the theoretical calculations are extracted from a statistical image analysis of the SEM images shown on the right (the scale bars represent 1.5 μm). Specifically, for (a) $D = 171$ nm, $a = 781$ nm, and $b = 389$ nm; for (b) $D = 204$ nm, $a = 781$ nm, $b = 389$ nm, and $d = 310$ nm; and for (c) $D = 208$ nm, $a = 781$ nm, $b = 389$ nm, and $d = 391$ nm. In all of the cases, the thickness of the gold film is $t = 80$ nm.

which is quantified by the uncertainty in the estimation of the refractive index $\Delta n \equiv \sqrt{\langle n^2 \rangle - \langle n \rangle^2}$. Since, in our particular case, we detect refractive-index changes through the measurement of the reflectance of the array, we can write the sensitivity of a single measurement as [40]

$$S = \frac{1}{\Delta n} = \frac{1}{\Delta R} \left| \frac{\partial R}{\partial \lambda} \right| \left| \frac{\partial \lambda}{\partial n} \right|. \quad (1)$$

Here, ΔR is the uncertainty in the estimation of reflectance, $\partial R/\partial \lambda$ is the slope of the reflectance spectrum, and $\partial \lambda/\partial n$ quantifies the variation of the optical response of the array with a change in n.

The value of ΔR is fundamentally limited by the quantum Cramér-Rao bound (QCRB), which provides the lowest possible uncertainty in the estimation of a parameter irrespective of the detection technique. The QCRB depends on the response of the system and the properties of the light that is used to probe it. When a coherent state of light is used, the sensitivity is limited by the shot-noise limit [25]. This limit can only be surpassed through the use of quantum correlated states of light, such as entangled or squeezed states [40]. Here, we analyze the effect on the sensitivity of using a bright two-mode squeezed state (BTMSS) [52] of light in a configuration in which one of

the modes probes the nanohole array and the other one is used as a reference [42]. The use of bright quantum states of light constitutes a good choice from a practical perspective as the sensitivity scales with the number of probing photons [53]. Although a Fock state [54] or a vacuum two-mode squeezed state [55] can make better use of quantum resources, it is difficult to generate them with a power large enough to actually surpass the absolute sensitivities achieved by classical devices [56–58]. The quantum correlations in a BTMSS are characterized by the squeezing parameter ζ, which is determined by the gain and efficiency of the nonlinear parametric process used to create it [52]. Neglecting all of the losses external to the sensor, the QCRB for the estimation of the reflectance in the configuration considered here is given by [53]

$$\Delta R^{\text{BTMSS}} = \sqrt{\frac{R - R^2 \left[1 - \text{sech}(2\zeta) \right]}{N}},$$

where N is the number of photons used to probe the sensor. The fundamental sensitivity bound of the nanohole arrays results from an interplay between their reflection spectra and the QCRB for the estimation of reflection ΔR^{BTMSS} [59], and can be calculated with Eq. (1).

Figure 4(a) displays the spectrum of the fundamental sensitivity bound normalized to $\sqrt{N}$ (left axis, solid curves) for the one- (orange curves) and two-hole array (green curves) when illuminated by one of the modes of the BTMSS while the other mode is used as a reference. In particular, we focus on the one- and two-hole arrays of Fig. 1(c) with $a = 784$ nm, $b = a/2$, $t = 80$ nm, $D = 210$ nm, and $d = 315$ nm. We extract $\partial R/\partial \lambda$ directly from the reflectance spectra of Fig. 1(c), and calculate $\partial \lambda/\partial n$ by repeating the corresponding calculations replacing the air above the arrays with a medium of refractive index $1 + \delta n$ with $\delta n \ll 1$. Notice that, as shown in Fig. 5, $\partial \lambda/\partial n$ is effectively constant for the one- and two-hole arrays in the range of wavelengths under consideration. We consider two different values for the squeezing parameter: $\zeta = 0$ (dark curves), which corresponds to a coherent state and determines the shot-noise limit, and $\zeta = 2$ (light curves). A squeezing parameter of $\zeta = 2$ corresponds to approximately -15 dB of intensity difference squeezing, which represents a high but experimentally attainable level of squeezing [60]. As anticipated from our previous analysis, the two-hole array achieves sensitivities more than 2 times larger than its one-hole counterpart. This can be directly attributed to the steeper slope of its reflectance spectrum. Indeed, comparing the sensitivity with the reflectance spectra of the arrays, which is shown with dashed curves (right scale), we observe that the wavelength at which the maximum sensitivity occurs is not at the resonance or at the maximum transmission, but results from an interplay between the slope of the reflectance and the reflection QCRB [59]. Furthermore, comparing the results obtained
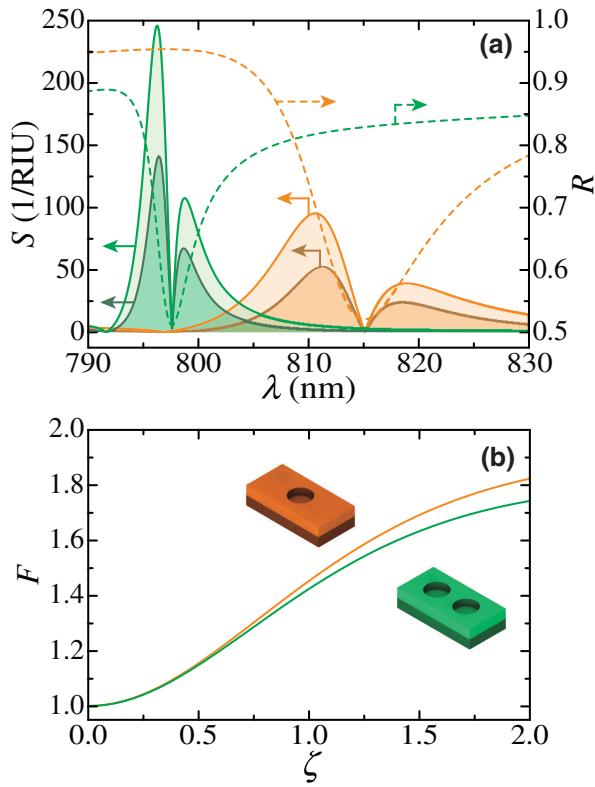
FIG. 4. (a) Sensitivity normalized to $\sqrt{N}$, where N is the number of probing photons, (left axis, solid curves) for the one- (orange curves) and the two-hole (green curves) arrays, as a function of wavelength when probed with a BTMSS. Dark and light curves correspond to values of the squeezing parameter $\zeta = 0$ (which corresponds to a coherent state) and $\zeta = 2$, respectively. The geometrical parameters of the arrays are those of Fig. 1(c): $a = 784$ nm, $b = a/2$, $t = 80$ nm, $D = 210$ nm, and $d = 315$ nm. For reference, we plot the reflectance of the arrays with dashed curves using the right axis. (b) Quantum enhancement factor, F, as a function of ζ for the two arrays of panel (a).

for $\zeta = 0$ (dark curves) and $\zeta = 2$ (light curves), we conclude that the sensitivity is increased by almost a factor of 2 when probing the nanohole array with a BTMSS instead of a coherent state. This enhancement is analyzed in more detail in Fig. 4(b), where we plot the quantum enhancement factor F. This quantity is defined as the ratio of the spectral maximum of the sensitivity bounds achieved with and without squeezing,

$$ F(\zeta) = \frac{\max_\lambda S(\zeta)}{\max_\lambda S(0)}. $$

Examining the results of Fig. 4(b), we observe that as ζ grows from 0 to 2, F approaches a value of approximately 1.8. Interestingly, the one-hole array shows a slightly larger F. This is the result of the dependence of the sensitivity on the slope of the reflectance and the reflectivity QCRB, which degrades with lower reflection. As can be seen from
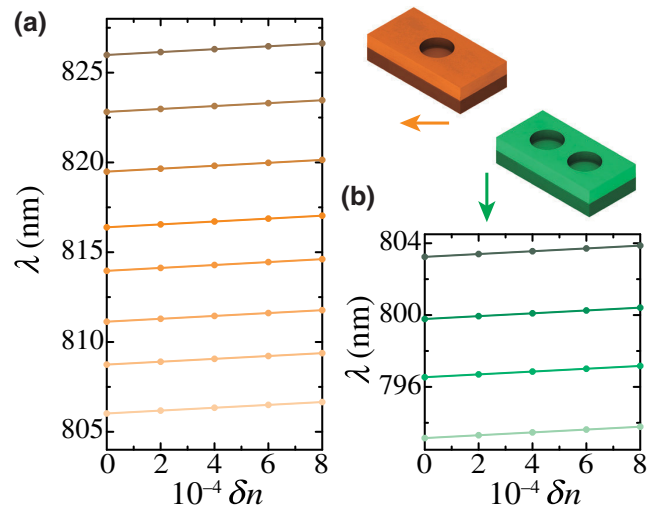

FIG. 5. Shift in the wavelength corresponding to a constant value of reflectance as a function of the change in the refractive index of the environment above the array, which is defined as $n = 1 + \delta n$. Panels (a) and (b) show the results for the one- and two-hole arrays, respectively. The geometrical parameters of the arrays are as in Fig. 4: $a = 784$ nm, $b = a/2$, $t = 80$ nm, $D = 210$ nm, and $d = 315$ nm. Examining the results of panels (a) and (b), we observe that, for both arrays, the slope of the curves, which corresponds to $\partial\lambda/\partial n$ appearing in Eq. (1), is effectively constant within the range of wavelengths under consideration. In particular, it takes the values $\partial\lambda/\partial n \cong 824$ nm and $\partial\lambda/\partial n \cong 796$ nm for the one- and two-hole arrays, respectively.

Fig. 4(a), while the two-hole array has a steeper slope, the one-hole array has a larger reflectance at its wavelength of maximum sensitivity. However, we emphasize that the two-hole array shows a larger absolute sensitivity for all values of ζ.

To complete our study, we compute the expected sensitivities for the experimental samples discussed in Figs. 3(a) and 3(b). In order to minimize the effect of the noise of the measured spectra on the calculation, we fit the measured reflectance using a cubic spline. The results of the fitting as well as the experimental reflectance spectra are plotted in Fig. 6 using the right axis with dashed curves and light solid curves, respectively. The orange curves denote the one-hole array, with parameters $D = 171$ nm, $a = 781$ nm, and $b = 389$ nm, while the green curves show the results for the two-hole array with parameters $D = 204$ nm, $a = 781$ nm, $b = 389$ nm, and $d = 310$ nm. Assuming, again, that these samples are probed with a BTMSS with a squeezing parameter ζ, we calculate the first two terms in Eq. (1) using the fitted reflectance data. For $d\lambda/dn$, we use the values extracted from Fig. 5, since the required measurements could not be performed with our experimental setup. The results of the sensitivity are shown in Fig. 6 using the left axis. The dark and light
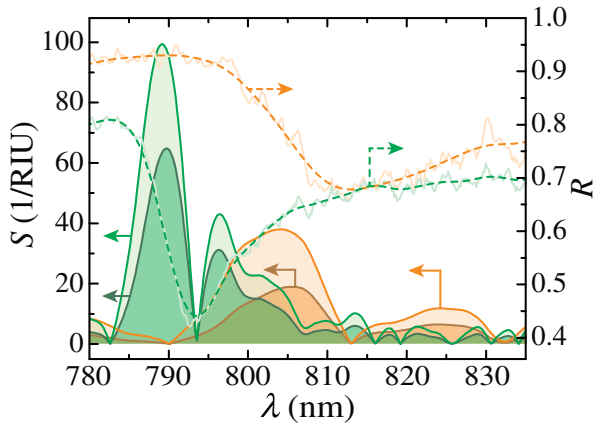
FIG. 6. Predicted experimental sensitivity for the arrays studied in Figs. 3(a) and 3(b), normalized to $\sqrt{N}$ (left axis, solid curves) as a function of wavelength when probed with a BTMSS. The orange curves correspond to the one-hole array of Fig. 3(a), while the green ones display the results for the two-hole array of Fig. 3(b). In all cases, dark and light curves correspond to values of the squeezing parameter $\zeta = 0$ and $\zeta = 2$, respectively. The geometrical parameters of the arrays are $D = 171$ nm, $a = 781$ nm, and $b = 389$ nm (one-hole array, orange curves) and $D = 204$ nm, $a = 781$ nm, $b = 389$ nm, and $d = 310$ nm (two-hole array, green curves). For reference, we plot the experimentally measured reflectance spectra of the arrays with light solid curves using the right axis, along with the corresponding cubic spline fits overlaid with dashed curves.

curves correspond to $\zeta = 0$ and $\zeta = 2$, respectively. Analyzing these results, we conclude that the enhancements are very similar to the theoretical predictions of Fig. 4 with overall lower sensitivities, as expected from the broader resonances and lower reflectance achieved experimentally.

III. CONCLUSIONS

In summary, we investigate the use of the lattice resonances supported by periodic arrays of nanoholes perforated in metallic films for quantum enhanced sensing. To that end, we perform a comprehensive theoretical analysis of the optical response of nanohole arrays with either one or two holes per unit cell. We show that both of these systems support strong lattice resonances that give rise to narrow dips in their reflectance spectrum and analyze how their characteristics depend on the different geometrical parameters. We find that the interplay between the size of the holes and their separation results in the two-hole arrays displaying a sharper and more pronounced dip in the reflectance spectrum, which, in addition to providing an extra parameter to tune their response, makes them better suited for sensing applications. We confirm these predictions through the fabrication and measurement of the reflectance of sample nanohole arrays. To complete our study, we perform a theoretical analysis of the fundamental bounds for the sensitivity to changes in the dielectric

environment that these nanohole arrays can achieve when probed with classical and squeezed states of light. We find that the two-hole arrays reach sensitivities more than double those of their one-hole counterparts. In all cases, the sensitivity is enhanced by a factor close to 2 when the arrays are probed with light in a BTMSS with a squeezing parameter of 2. The results of this work advance our understanding of the response of periodic arrays of nanoholes and pave the way to use them as sensors capable of exploiting the quantum resources of squeezed light to achieve detection thresholds beyond the classical limit.

APPENDIX A: ELECTROMAGNETIC CALCULATIONS

All of the electromagnetic calculations presented in this work are obtained from the rigorous solutions of Maxwell's equations using a FEM approach implemented in the commercial software COMSOL Multiphysics. In all cases, we assume the array to be placed in the x-y plane with the silicon substrate below (i.e., $z < 0$) and the origin located at the center of the hole, for the one-hole arrays, and at the center of the line connecting the holes, for the two-hole array. We use tabulated data taken from Refs. [61] and [62] for the dielectric functions of gold and silicon, respectively. The arrays are excited by a plane wave propagating along the negative z axis with the magnetic field polarized parallel to the y axis. Due to the periodicity of the system, we need to simulate one unit cell with periodic boundary conditions. However, we exploit the fact that, for both the one- and two-hole arrays, the unit cell has a fourfold reflection symmetry with respect to the x-z and y-z planes. This allows us to restrict the simulation domain to one quarter of the total unit cell. Therefore, we choose the boundaries of the simulation domain parallel to the x-z and y-z planes to be perfect magnetic and perfect

electric conductors, respectively, while in the direction parallel to the z axis the domain is truncated using perfectly matched layers (PMLs) to simulate an extended space. Upon solving Maxwell's equations, we obtain the value of the electric and magnetic fields at all points in the simulation domain and use them to calculate the total power leaving the simulation domain along the positive and negative z axis. Using these values, normalized to the power of the incident plane wave, we compute the reflectance and transmittance of the array. Each calculation is checked for convergence with respect to the mesh and simulation domain sizes.

APPENDIX B: FABRICATION OF NANOHOLE ARRAYS

The nanohole arrays are fabricated on 1–10 Ohm cm p-type (100) silicon with 35-nm thermal oxide using electron-beam lithography (EBL) and metal lift off. We use 4% polymethyl methacrylate with molecular weight 950 000 in anisole as the EBL resist. After spin coating at 5000 rpm for 30 s, the EBL resist is baked at 170 °C for 5 min. Positive tone EBL is performed using a 30-kV scanning electron microscope. After electron-beam exposure, the pattern is developed out using methyl isobutyl ketone and isopropyl alcohol 1:3 for 60 s. After descum in oxygen plasma, a stack of 2 nm Ti/80 nm Au is deposited in an electron gun evaporator. The sample is then soaked in acetone for lift off.

APPENDIX C: REFLECTANCE MEASUREMENTS

The reflectance spectra of the fabricated nanohole arrays are measured with a white-light spectroscopy setup. As shown in Fig. 7, light from a broadband halogen lamp (Osram 64641-HLX-G6.35, $\lambda = 550$ nm $- 1100$ nm) is coupled into a multimode broadband fiber (Ocean Optics P1000-2-VIS-NIR) to obtain uniform illumination at the output of the fiber. Since the response of the nanohole

arrays is polarization dependent, we use a Glan-Thompson polarizer (GT) to linearly polarize the light after the fiber. The electric field polarization of the light is then aligned to the x axis, along which the symmetry is broken for the two-hole arrays as defined in Fig. 1, with a broadband half-wave plate ($\lambda/2$). We then use a 4-f optical system, composed of two achromatic lenses, L_1 and L_2, with focal lengths $f_1 = 400$ mm and $f_2 = 30$ mm, respectively, to demagnify and image the fiber output tip (1 mm diameter) to the plasmonic nanohole structure (size of 120 μm $\times$ 120 μm). Finally, we use a one-to-one optical system composed of a lens, L_3, with focal length $f_3 = 30$ mm to allow enough space for the necessary translation stages to mount and align the nanohole array to the probing white light. This optical system produces an image of the output tip of the fiber at the array with a size (waist diameter) of 75 μm. Given that the sharp response of the lattice resonances is due to a collective plasmonic effect, excitation with a field close to a plane wave is needed. Therefore, an iris is placed at the Fourier plane of the 4-f optical system (400 mm to the right of L_1) to filter the high spatial frequencies (k vectors) of the light from the multimode fiber.

The probing light is reflected from the plasmonic structure and retraces its own path. To separate it from the incident light, a broadband balanced 50:50 beam splitter is placed between the half-wave plate and the 4-f optical system, as shown in Fig. 7, to pick off half of the reflected light. The light is then fiber coupled to a CCD spectrometer (Thorlabs model CCS100) to measure its spectrum. For all the measurements, the integration time of the spectrometer is kept at 500 ms and the measured spectra are averaged 100 times.

The silicon substrate on which the nanohole arrays are fabricated is designed to contain a region with a uniform gold film of the same thickness and dimensions as the gold film used for the arrays. The reflectance spectrum from the uniform gold film serves as the reference to eliminate
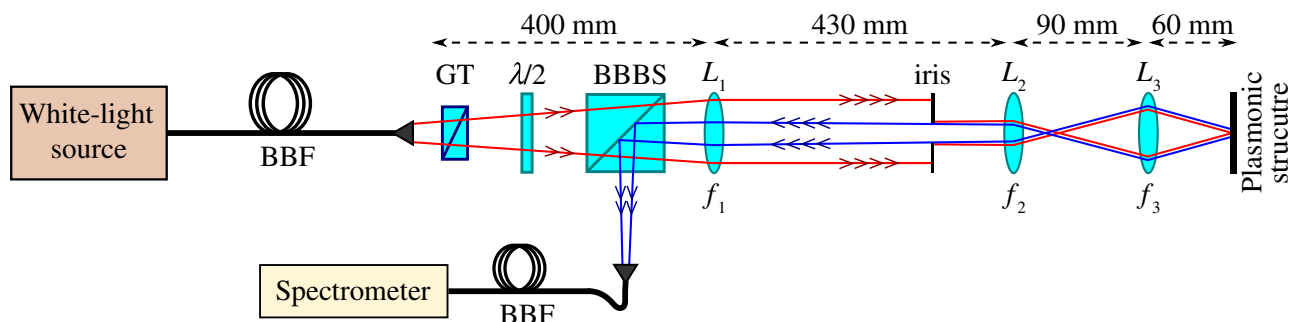

FIG. 7. Experimental white-light spectroscopy setup for the characterization of the reflectance spectrum of nanohole arrays. GT, Glan-Thompson polarizer; BBF, broadband fiber; BBBS, broadband balanced (50:50) beam splitter; $\lambda/2$, broadband half-wave plate; L_i, achromatic lens. The lenses used for the 4-f optical system, L_1 and L_2, have focal lengths $f_1 = 400$ mm and $f_2 = 30$ mm, respectively, while the one used for the one-to-one imaging system, L_3, has a focal length $f_3 = 30$ mm. The iris is placed at the Fourier plane of the white-light fiber output tip.

the effects of optical losses in the characterization system. Measurements with the white-light spectroscopy setup described above are performed for the light reflected from the reference gold layer and the nanohole structures. The ratio of these measurements is then calculated to obtain the normalized reflectance spectra for the nanohole arrays shown in Fig. 3.

---

[1] F. J. García de Abajo, Colloquium: Light scattering by particle and hole arrays, Rev. Mod. Phys. **79,** 1267 (2007).

[2] F. J. Garcia-Vidal, L. Martin-Moreno, T. W. Ebbesen, and L. Kuipers, Light passing through subwavelength apertures, Rev. Mod. Phys. **82,** 729 (2010).

[3] T. Rindzevicius, Y. Alaverdyan, B. Sepulveda, T. Pakizeh, M. Käll, R. Hillenbrand, J. Aizpurua, and F. J. García de Abajo, Nanohole plasmons in optically thin gold films, J. Phys. Chem. C **111,** 1207 (2007).

[4] T. W. Ebbesen, H. J. Lezec, H. F. Ghaemi, T. Thio, and P. A. Wolff, Extraordinary optical transmission through sub-wavelength hole arrays, Nature **391,** 667 (1998).

[5] L. Martín-Moreno, F. J. García-Vidal, H. J. Lezec, K. M. Pellerin, T. Thio, J. B. Pendry, and T. W. Ebbesen, Theory of Extraordinary Optical Transmission through Subwavelength Hole Arrays, Phys. Rev. Lett. **86,** 1114 (2001).

[6] S. G. Rodrigo, F. J. García-Vidal, and L. Martín-Moreno, Influence of material properties on extraordinary optical transmission through hole arrays, Phys. Rev. B **77,** 075401 (2008).

[7] H. A. Bethe, Theory of diffraction by small holes, Phys. Rev. **66,** 163 (1944).

[8] A. G. Brolo, S. C. Kwok, M. G. Moffitt, R. Gordon, J. Riordon, and K. L. Kavanagh, Enhanced fluorescence from arrays of nanoholes in a gold film, J. Am. Chem. Soc. **127,** 14936 (2005).

[9] M. Saboktakin, X. Ye, U. K. Chettiar, N. Engheta, C. B. Murray, and C. R. Kagan, Plasmonic enhancement of nanophosphor upconversion luminescence in Au nanohole arrays, ACS Nano **7,** 7186 (2013).

[10] F. Cheng, J. Gao, T. S. Luk, and X. Yang, Structural color printing based on plasmonic metasurfaces of perfect light absorption, Sci. Rep. **5,** 11045 (2015).

[11] Y. Lee, M.-K. Park, S. Kim, J. H. Shin, C. Moon, J. Y. Hwang, J.-C. Choi, H. Park, H.-R. Kim, and J. E. Jang, Electrical broad tuning of plasmonic color filter employing an asymmetric-lattice nanohole array of metasurface controlled by polarization rotator, ACS Photonics **4,** 1954 (2017).

[12] M. Najiminaini, F. Vasefi, B. Kaminska, and J. J. L. Carson, Nanohole-array-based device for 2D snapshot multispectral imaging, Sci. Rep. **3,** 2589 (2013).

[13] J. A. H. van Nieuwstadt, M. Sandtke, R. H. Harmsen, F. B. Segerink, J. C. Prangsma, S. Enoch, and L. Kuipers, Strong Modification of the Nonlinear Optical Response of Metallic Subwavelength Hole Arrays, Phys. Rev. Lett. **97,** 146102 (2006).

[14] R. Gordon, D. Sinton, K. L. Kavanagh, and A. G. Brolo, A new generation of sensors based on extraordinary optical transmission, Acc. Chem. Res. **41,** 1049 (2008).

[15] G. A. Cervantes Tellez, A. Ahmed, and R. Gordon, Optimizing the resolution of nanohole arrays in metal films for refractive-index sensing, App. Phys. A **109,** 775 (2012).

[16] G. A. Cervantes Tellez, S. Hassan, R. N. Tait, P. Berini, and R. Gordon, Atomically flat symmetric elliptical nanohole arrays in a gold film for ultrasensitive refractive index sensing, Lab Chip **13,** 2541 (2013).

[17] C. Escobedo, On-chip nanohole array based sensing: A review, Lab Chip **13,** 2445 (2013).

[18] A.-P. Blanchard-Dionne and M. Meunier, Sensing with periodic nanohole arrays, Adv. Opt. Photon **9,** 891 (2017).

[19] A. Hajebifard and P. Berini, Fano resonances in plasmonic heptamer nano-hole arrays, Opt. Express **25,** 18566 (2017).

[20] A. Prasad, J. Choi, Z. Jia, S. Park, and M. R. Gartia, Nanohole array plasmonic biosensors: Emerging point-of-care applications, Biosens. Bioelectron **130,** 185 (2019).

[21] A. Hajebifard, C. Hahn, J. Walia, H. Suleman, F. Variola, A. Weck, and P. Berini, Fano resonances in nanohole oligomers in a gold film, J. Appl. Phys. **129,** 033103 (2021).

[22] A. E. Cetin, D. Etezadi, B. C. Galarreta, M. P. Busson, Y. Eksioglu, and H. Altug, Plasmonic nanohole arrays on a robust hybrid substrate for highly sensitive label-free biosensing, ACS Photonics **2,** 1167 (2015).

[23] A. A. Yanik, M. Huang, O. Kamohara, A. Artar, T. W. Geisbert, J. H. Connor, and H. Altug, An optofluidic nanoplasmonic biosensor for direct detection of live viruses from biological media, Nano Lett. **10,** 4962 (2010).

[24] X. Wang, M. Jefferson, P. C. D. Hobbs, W. P. Risk, B. E. Feller, R. D. Miller, and A. Knoesen, Shot-noise limited detection for surface plasmon sensing, Opt. Express **19,** 107 (2011).

[25] V. Giovannetti, S. Lloyd, and L. Maccone, Quantum-enhanced measurements: Beating the standard quantum limit, Science **306,** 1330 (2004).

[26] M. A. Taylor and W. P. Bowen, Quantum metrology and its application in biology, Phys. Rep. **615,** 1 (2016).

[27] M. A. Taylor, J. Janousek, V. Daria, J. Knittel, B. Hage, H.-A. Bachor, and W. P. Bowen, Biological measurement beyond the quantum limit, Nat. Photon **7,** 229 (2013).

[28] C. M. Caves, Quantum-mechanical noise in an interferometer, Phys. Rev. D **23,** 1693 (1981).

[29] M. Xiao, L.-A. Wu, and H. J. Kimble, Precision Measurement beyond the Shot-Noise Limit, Phys. Rev. Lett. **59,** 278 (1987).

[30] The LIGO Scientific Collaboration, A gravitational wave observatory operating beyond the quantum shot-noise limit, Nat. Photon **7,** 962 (2011).

[31] M. Tse, H. Yu, N. Kijbunchoo, A. Fernandez-Galiana, P. Dupej, L. Barsotti, C. D. Blair, D. D. Brown, S. E. Dwyer, and A. Effler, et al., Quantum-Enhanced Advanced LIGO Detectors in the era of Gravitational-Wave Astronomy, Phys. Rev. Lett. **123,** 231107 (2019).

[32] E. Altewischer, M. P. van Exter, and J. P. Woerdman, Plasmon-assisted transmission of entangled photons, Nature **418,** 304 (2002).

[33] E. Moreno, F. J. García-Vidal, D. Erni, J. I. Cirac, and L. Martín-Moreno, Theory of Plasmon-Assisted Transmission of Entangled Photons, Phys. Rev. Lett. **92,** 236801 (2004).

[34] S. Fasel, F. Robin, E. Moreno, D. Erni, N. Gisin, and H. Zbinden, Energy-Time Entanglement Preservation in

Plasmon-Assisted Light Transmission, Phys. Rev. Lett. **94,** 110501 (2005).

[35] B. J. Lawrie, P. G. Evans, and R. C. Pooser, Extraordinary Optical Transmission of Multimode Quantum Correlations via Localized Surface Plasmons, Phys. Rev. Lett. **110,** 156802 (2013).

[36] M. W. Holtfrerich, M. Dowran, R. Davidson, B. J. Lawrie, R. C. Pooser, and A. M. Marino, Toward quantum plasmonic networks, Optica **3,** 985 (2016).

[37] D. A. Kalashnikov, Z. Pan, A. I. Kuznetsov, and L. A. Krivitsky, Quantum Spectroscopy of Plasmonic Nanostructures, Phys. Rev. X **4,** 011049 (2014).

[38] R. C. Pooser and B. Lawrie, Plasmonic trace sensing below the photon shot noise limit, ACS Photonics **3,** 8 (2016).

[39] C. Lee, F. Dieleman, J. Lee, C. Rockstuhl, S. A. Maier, and M. Tame, Quantum plasmonic sensing: Beyond the shot-noise and diffraction limit, ACS Photonics **3,** 992 (2016).

[40] B. J. Lawrie, P. D. Lett, A. M. Marino, and R. C. Pooser, Quantum sensing with squeezed light, ACS Photonics **6,** 1307 (2019).

[41] C. Lee, B. Lawrie, R. Pooser, K.-G. Lee, C. Rockstuhl, and M. Tame, Quantum plasmonic sensors, Chem. Rev. **121,** 4743 (2021).

[42] M. Dowran, A. Kumar, B. J. Lawrie, R. C. Pooser, and A. M. Marino, Quantum-enhanced plasmonic sensing, Optica **5,** 628 (2018).

[43] S. Baur, S. Sanders, and A. Manjavacas, Hybridization of lattice resonances, ACS Nano **12,** 1618 (2018).

[44] A. Manjavacas, L. Zundel, and S. Sanders, Analysis of the limits of the near-field produced by nanoparticle arrays, ACS Nano **13,** 10682 (2019).

[45] M. Rudé, V. Mkhitaryan, A. E. Cetin, T. A. Miller, A. Carrilero, S. Wall, F. J. G. de Abajo, H. Altug, and V. Pruneri, Ultrafast and broadband tuning of resonant optical nanostructures using phase-change materials, Adv. Opt. Mater. **4,** 1060 (2016).

[46] A. Cuartero-González, S. Sanders, L. Zundel, A. I. Fernández-Domínguez, and A. Manjavacas, Super- and subradiant lattice resonances in bipartite nanoparticle arrays, ACS Nano **14,** 11876 (2020).

[47] L. Zundel, A. May, and A. Manjavacas, Lattice resonances induced by periodic vacancies in arrays of nanoparticles, ACS Photonics **8,** 360 (2021).

[48] W. Zhao, H. Jiang, B. Liu, Y. Jiang, C. Tang, and J. Li, Fano resonance based optical modulator reaching 85% modulation depth, Appl. Phys. Lett. **107,** 171109 (2015).

[49] K. Koshelev, G. Favraud, A. Bogdanov, Y. Kivshar, and A. Fratalocchi, Nonradiating photonics with resonant dielectric nanostructures, Nanophotonics **8,** 725 (2019).

[50] M.-S. Hwang, H.-R. Kim, K.-Y. Jeong, H.-G. Park, and Y. Kivshar, Novel non-plasmonic nanolasers empowered by topology and interference effects, Nanophotonics **10,** 3599 (2021).

[51] L. Zundel and A. Manjavacas, Finite-size effects on periodic arrays of nanostructures, J. Phys.: Photonics **1,** 015004 (2019).

[52] C. F. McCormick, A. M. Marino, V. Boyer, and P. D. Lett, Strong low-frequency quantum correlations from a four-wave-mixing amplifier, Phys. Rev. A **78,** 043816 (2008).

[53] T. S. Woodworth, K. W. C. Chan, C. Hermann-Avigliano, and A. M. Marino, Transmission estimation at the Cramér-Rao bound for squeezed states of light in the presence of loss and imperfect detection, Phys. Rev. A **102,** 052603 (2020).

[54] G. Adesso, F. Dell'Anno, S. De Siena, F. Illuminati, and L. A. M. Souza, Optimal estimation of losses at the ultimate quantum limit with non-Gaussian states, Phys. Rev. A **79,** 040305 (2009).

[55] C. Invernizzi, M. G. A. Paris, and S. Pirandola, Optimal detection of losses by thermal probes, Phys. Rev. A **84,** 022334 (2011).

[56] M. Uria, P. Solano, and C. Hermann-Avigliano, Deterministic Generation of Large Fock States, Phys. Rev. Lett. **125,** 093603 (2020).

[57] I. N. Agafonov, M. V. Chekhova, and G. Leuchs, Two-color bright squeezed vacuum, Phys. Rev. A **82,** 011801 (2010).

[58] M. Chekhova, G. Leuchs, and M. Żukowski, Bright squeezed vacuum: Entanglement of macroscopic light beams, Opt. Commun. **337,** 27 (2015).

[59] M. Dowran, T. S. Woodworth, A. Kumar, and A. M. Marino, Fundamental sensitivity bounds for quantum enhanced optical resonance sensors based on transmission and phase estimation, Quantum Sci. Technol. **7,** 015011 (2022).

[60] H. Vahlbruch, M. Mehmet, K. Danzmann, and R. Schnabel, Detection of 15 dB Squeezed States of Light and Their Application for the Absolute Calibration of Photoelectric Quantum Efficiency, Phys. Rev. Lett. **117,** 110801 (2016).

[61] P. B. Johnson and R. W. Christy, Optical constants of the noble metals, Phys. Rev. B **6,** 4370 (1972).

[62] D. E. Aspnes and A. A. Studna, Dielectric functions and optical parameters of Si, Ge, GaP, GaAs, GaSb, InP, InAs, and InSb from 1.5 to 6.0 eV, Phys. Rev. B **27,** 985 (1983).